Published in final edited form as:
Magn Reson Med. 2010 May ; 63(5): 1210–1218. doi:10.1002/mrm.22288.

3D Magnetization-Prepared Imaging Using a Stack-of-Rings Trajectory

Holden H. Wu and **Dwight G. Nishimura**
Magnetic Resonance Systems Research Laboratory, Department of Electrical Engineering, Stanford University, Stanford, California.

Abstract

Efficient acquisition strategies for magnetization-prepared imaging based on the 3D stack-of-rings *k*-space trajectory are presented in this work. The 3D stack-of-rings can be acquired with centric ordering in all three dimensions for greater efficiency in capturing the desired contrast. In addition, the 3D stack-of-rings naturally supports spherical coverage in *k*-space for shorter scan times while achieving isotropic spatial resolution. While non-Cartesian trajectories generally suffer from greater sensitivity to system imperfections, the 3D stack-of-rings can enhance magnetization-prepared imaging with a high degree of robustness to timing delays and off-resonance effects. As demonstrated with phantom scans, timing errors and gradient delays only cause a bulk rotation of the 3D stack-of-rings reconstruction. Furthermore, each ring can be acquired with a time-efficient retracing design to resolve field inhomogeneities and enable fat/water separation. To demonstrate its effectiveness, the 3D stack-of-rings are considered for the case of inversion-recovery-prepared structural brain imaging. Experimental results show that the 3D stack-of-rings can achieve higher signal-to-noise ratio (SNR) and higher contrast-to-noise ratio (CNR) within a shorter scan time when compared to the standard inversion-recovery-prepared sequence based on 3D Cartesian encoding. The design principles used for this specific case of inversion-recovery-prepared brain imaging can be applied to other magnetization-prepared imaging applications.

Keywords

concentric rings; 3D stack-of-rings; 3D imaging; magnetization preparation; water-fat decomposition

Introduction

Three dimensional magnetization-prepared imaging is a versatile but challenging imaging paradigm that aims to capture high tissue contrast over an entire imaging volume within a short scan duration. The core concept of magnetization-prepared imaging is the combined use of preparation modules for generating contrast and rapid readout modules for acquisition (1,2). Most often, the readout module is based on a gradient-echo (GRE) sequence, but other sequences, such as fast spin-echo (FSE), can also be used for acquisition. Different preparation modules can be employed to achieve the desired image contrast. For example, magnetization-prepared sequences have been applied for both T_1-weighted (2–7) and T_2-weighted imaging (8), MR angiography (9), black-blood cardiac imaging (10), and also to facilitate exams that administer exogenous contrast material (11,12).

Address correspondence to: Holden H. Wu, Packard Electrical Engineering, Room 208, 350 Serra Mall, Stanford, CA 94305-9510, TEL: (650) 723-3810, holdenhwu@stanford.edu.

Similar to all other MR imaging applications, magnetization-prepared imaging sequences must balance the competing objectives of broad spatial field-of-view (FOV), fine spatial resolution, high signal-to-noise ratio (SNR), high tissue contrast-to-noise ratio (CNR), and short scan time. Magnetization-prepared imaging also has the additional challenge that prepared contrast is transient and can disappear quickly. If not properly accounted for, this signal transition can affect the final image SNR, CNR, and resolution. General MRI strategies such as employing multiple receiver elements or imaging at higher field strengths can certainly be adopted to provide a more favorable trade-off between the various imaging goals. Equally important for magnetization-prepared imaging, if not more, is the specific design of an efficient acquisition strategy that can capture as much of the intended contrast as possible in a smooth and time-efficient manner. Methods such as *k*-space segmentation (3,13) and centric ordering (6,14) are usually incorporated into the acquisition design to counter the potential loss of resolution caused by the transitory signal weighting and to maximize the image contrast.

In this work, we present efficient acquisition strategies for magnetization-prepared imaging based on the 3D stack-of-rings *k*-space trajectory. The 3D stack-of-rings inherits flexible trade-offs between image CNR, SNR, spatial resolution, and scan time from the 2D concentric rings (15–18) and extends these advantages to three dimensions. Furthermore, the 3D stack-of-rings can be acquired with centric ordering in all three spatial dimensions and naturally supports spherical coverage in 3D *k*-space for additional time savings while achieving isotropic spatial resolution. These advantages allow the 3D stack-of-rings to achieve higher SNR and CNR within a shorter scan duration when compared to a standard sequence based on 3D Cartesian (3DFT) encoding for the same imaging volume.

While the application of non-Cartesian trajectories is often hindered by their greater sensitivity to system imperfections, the 3D stack-of-rings can be employed with a high degree of robustness to timing delays and off-resonance effects. Timing errors and gradient delays which usually require additional calibration and processing for non-Cartesian imaging only cause a benign bulk rotation in the reconstruction of 3D stack-of-rings acquisitions. In addition, the unique circularly symmetric sampling nature of concentric rings enables a time-efficient retracing acquisition that resolves field inhomogeneity and supports fat/water separation (17, 18). We present *in vivo* brain images acquired with an inversion-recovery-prepared sequence to demonstrate that the 3D stack-of-rings enables efficient magnetization-prepared imaging.

Methods

3D Stack-of-Rings

A set of N uniformly spaced concentric rings (Fig. 1a) is used to encode (k_x, k_y) (15–17). Sinusoidal gradients are designed for the outermost ring (Fig. 1b), and then scaled down to acquire one ring after each RF excitation pulse (Fig. 1d) with the readout window length held constant for all rings. Spatial coverage is extended to 3D by adding a slice-encoding gradient (Fig. 1c). This gradient design for concentric rings results in a sampling density identical to 2D projection-reconstruction (PR) in (k_x, k_y) and ensures that timing errors and gradient delays only cause a bulk rotation in the reconstructed image. Phantom experiments were conducted to verify this property.

Although non-Cartesian imaging trajectories are sensitive to off-resonance effects caused by main field inhomogeneities and chemical shift, the unique circular sampling symmetry of the concentric rings allows each ring to be acquired with a time-efficient retracing method (Fig. 1b) that resolves these off-resonance effects. Similar to multi-echo acquisitions, each revolution Rev_m can be reconstructed individually to characterize the fat/water phase evolution difference at time point t_m (m = 1, 2, 3). Separate fat and water images can then be calculated from the retraced dataset.

Image reconstruction of the 3D stack-of-rings acquisition consists of a Fourier transform in k_z, followed by a series of 2D gridding operations for each slice (17). Water images are calculated for each slice by first demodulating each Rev_m at water frequency and then using the individual images thus reconstructed in an iterative multi-point Dixon algorithm (18,19). Fat images are obtained similarly by first demodulating at fat frequency (18). It is also possible to perform fat/water separation with a direct spectroscopic reconstruction in (k_x, k_y, k_z, t)-space (18). Data from multiple receiver elements are combined using a sum-of-squares.

Magnetization-Prepared Imaging With Rings

We have previously shown that the 2D concentric rings trajectory offers advantages for magnetization-prepared imaging – concentric rings are inherently centric-ordered, provide smooth weighting in *k*-space, and enable shorter scan times (17). The 3D stack-of-rings trajectory inherits these desirable properties and extends them to three dimensions. Compared to other 3D readout trajectories such as 3DFT, 3DPR, or 3D stack-of-spirals, 3D stack-of-rings can be acquired with centric ordering in three dimensions (Fig. 2). In addition, the geometry of the 3D stack-of-rings naturally supports spherical coverage in 3D *k*-space (Fig. 2) for enhanced time-efficiency while achieving isotropic spatial resolution (7,20). By starting from the center of 3D *k*-space and progressing outwards in all three dimensions, the 3D stack-of-rings trajectory acquires a sphere in the central region of *k*-space rapidly and compactly to capture the transient contrast with high efficiency. This isotropic distribution of signal transition also means that the potential spatial blurring in each individual dimension will be less severe than if signal transition were concentrated along one particular centric-ordering dimension.

IR-SPGR Brain Imaging with Rings

To demonstrate the effectiveness of the 3D stack-of-rings for magnetization-prepared imaging, we specifically considered an inversion-recovery-prepared RF-spoiled gradient-echo (IR-SPGR) sequence for T_1-weighted 3D brain imaging (2). The IR-SPGR sequence is often used to characterize brain morphology, enable tissue volume measurements, acquire the anatomical reference for functional brain imaging, and also to facilitate exogenous contrast-enhanced studies. The objectives of the IR-SPGR sequence for brain imaging are to achieve high spatial resolution (~1 mm isotropic), high white/gray matter contrast-to-noise ratio (CNR), and high SNR while keeping the scan time reasonably short (under ~10 min). The design principles and trade-offs involved for this particular sequence can be generalized to other magnetization-prepared imaging scenarios.

The IR-SPGR sequence (Fig. 3) acquires the desired set of *k*-space samples as P interleaved segments of Q encoding steps ($P \cdot Q$ = total number of encoding steps). After each preparatory inversion pulse and a specified inversion time (TI), Q encoding steps are acquired. Following acquisition, a recovery delay time (TD) is observed before repeating the next prepare-acquire-recover segment. Increasing Q enables shorter scans at the cost of diminished tissue CNR, while increasing P enhances CNR at the cost of longer scans. Q is typically set to around 100 to balance contrast and scan time (5–7). Parameters TI and TD may be increased to boost SNR and/or CNR, but results in longer scans.

In this work, we use the 3D stack-of-rings with spherical coverage (Fig. 2) for readout. A set of N = 120 rings encode (k_x, k_y) to achieve 1×1 mm^2 resolution over a 24 cm FOV (240×240 matrix). Slice-encoding gradients partition an 18-cm slab into 1-mm slices (180 slices) for volumetric coverage. The full set of encoding steps is first centric-ordered in three dimensions by sorting the rings according to their radial distance $\sqrt{k_x^2+k_y^2+k_z^2}$ from the origin of *k*-space. *k*-Space segmentation is then performed by arranging the encoding steps into interleaved

readout segments of $Q = 120$ rings each, where each segment starts its acquisition in the central region of 3D *k*-space and progresses outwards in all three dimensions. Since three-dimensional centric ordering is employed, there is only one acquisition loop for the Q encoding steps after each preparation pulse (Fig. 3). To achieve the prescribed FOV and resolution, a total of $P = 141$ interleaved segments are acquired. In general, Q does not have to be equal to N.

Other important parameters of the IR-SPGR sequence include the inversion angle β, readout TE and TR, and readout excitation angle θ. For our experiments, a hyperbolic-secant adiabatic π pulse (21) was used for uniform inversion over the volume of interest, thus β was fixed at 180°. The readout TE and TR are typically minimized, with TR on the order of 10 ms, to decrease scan time and preserve contrast. The minimum TE and TR for our specific 3D stack-of-rings trajectory are TE/TR = 2/12 ms. Excitation angle θ may be increased to boost SNR, but doing so can decrease overall CNR and introduce spatial blurring from increased signal modulation. Most often, θ is in the range of 5° to 20°.

IR-SPGR Sequence Design

To find values of TI, TD, and θ that balance CNR, SNR, and total scan time, we performed Bloch equation simulations over a relevant range of sequence parameters for gray matter (GM), white matter (WM), and cerebrospinal fluid (CSF). The relaxation and density parameters used in the simulations were GM/WM/CSF T_1 = 940/550/4300 ms, T_2 = 100/90/2000 ms, and ρ = 0.75/0.65/1.0 (22). In addition, we neglected relaxation effects during RF excitation and assumed perfect spoiling of transverse magnetization after the inversion pulse and before each excitation pulse (5–7).

Representative simulation results with TI/TD = 900/600 ms and Q/TE/TR/θ = 120/2 ms/12 ms/15° are plotted in Fig. 4 for the first five preparation segments. As seen in Fig. 4a, the signal evolution stabilizes after about two full cycles of the prepare-acquire-recover outer loop. The magnetization levels in Fig. 4 were normalized such that CSF magnetization at equilibrium equals 1. Signal evolution during acquisition is shown in Fig. 4b for the fifth segment. WM/GM signal difference starts out high due to preparation, but decays away with each successive readout. We found that the concentric rings are able to accommodate a slightly higher flip angle of θ = 15° to increase SNR while maintaining the desired image resolution.

A full set of simulations were then performed over the range of TI = 600–1200 ms (in steps of 50 ms) and TD = 0–1200 ms (in steps of 100 ms) for Q/TE/TR/θ = 120/2 ms/12 ms/15°. The signal levels M_{xy}(WM) and M_{xy}(GM) from the first encoding step of the readout segment were recorded and used to indicate SNR_{WM} and SNR_{GM}, respectively. For the range of TI and TD considered in these simulations, M_{xy}(WM) was generally greater than M_{xy}(GM). The WM/GM signal difference was normalized with respect to M_{xy}(WM) to give a contrast efficiency ratio η:

$$\eta = \left| M_{xy}(\mathrm{WM}) - M_{xy}(\mathrm{GM}) \right| / M_{xy}(\mathrm{WM}) \propto \mathrm{CNR}/\mathrm{SNR}_{WM} \quad (1)$$

This measure η characterizes WM/GM contrast as a ratio that is independent of noise level and also indicates the efficiency by which an overall increase in signal level is translated into CNR. Since there is an inherent trade-off between SNR_{WM}, SNR_{GM}, and CNR, a practical approach for selecting TI and TD is to aim for sufficient M_{xy}(WM) while maintaining a moderate η.

Figures 5a and 5c plot M_{xy}(WM) and η over the range of simulated TI and TD, respectively. Increasing TI for a fixed TD increases the signal level while decreasing the contrast efficiency. On the other hand, increasing TD for a fixed TI lowers the signal level while raising the contrast efficiency. The results in Fig. 5a and 5c are reformatted as contour plots in Fig. 5b and 5d to

include the corresponding scan time T_{scan} for whole-brain coverage (P = 141 segments). Two dots in the contour plots represent two protocol designs that achieve good balance between SNR, CNR, and scan time. Protocol **A** (TI/TD = 600/0 ms, T_{scan} = 4 min 52 s) is a fast scan that covers the whole brain in under 5 minutes, while protocol **B** (TI/TD = 900/600 ms, T_{scan} = 7 min) achieves higher SNR with a slightly longer scan. Both protocols theoretically achieve η ~ 30%, which is similar to the value calculated from the experimental results reported by other researchers (5–7).

Image Analysis

We performed region-of-interest (ROI) SNR and CNR analysis based on the reconstructed magnitude images. Noise standard deviation σ was measured from an ROI containing only background (23):

$$\sigma \approx \sqrt{\frac{\sum_{i=1}^{L} (\text{pixel value})_i^2}{2 \cdot L \cdot E}} \quad (2)$$

where L represents the number of pixels in the ROI and E denotes the number of receiver elements. Average signal $\bar{M}$ was measured for gray matter (GM) and white matter (WM). Since $\bar{M}/\sigma > 10$ in our experiments, a fixed correction factor of 1 was subtracted to obtain the SNR (23):

$$\text{SNR} = \bar{M}/\sigma - 1 \quad (3)$$

This resulted in a slight underestimation for cases of high SNR. White/gray matter CNR was calculated as the difference between SNR_{WM} and SNR_{GM}.

Results

Experiments were performed on a GE Signa 1.5 T Excite system with maximum gradient amplitude of 40 mT/m and maximum slew rate of 150 mT/m/ms. TE for the concentric rings is defined as the time between the peak of the RF excitation and the first readout sample. Informed consent was obtained before scanning all subjects.

Timing Delay Phantom Results

We imaged a phantom in a birdcage head coil to assess the effects of timing delays on the 2D concentric rings trajectory, on which the 3D stack-of-rings is based. The gradient-to-acquisition delay was intentionally varied from the default calibrated value to emulate timing delays that arise from gradient delays, timing errors, and also the first-order effects of eddy currents. The concentric rings gradient design for this experiment supported a 20 cm FOV and isotropic in-plane resolution of 1 mm. All rings were sampled with a single revolution. A 5 mm slice was acquired using an SPGR sequence with parameters TE/TR/θ = 2 ms/6.8 ms/30° and readout bandwidth of ±125 kHz (4 μs/sample). Images were reconstructed with no correction for the introduced delays.

When the default gradient-to-acquisition delay was used, the phantom image was faithfully reconstructed (Fig. 6a), as expected. The phantom is slightly tilted in the FOV due to the actual placement in the head coil and not due to delays. With a gradient-to-acquisition delay of +8 samples (32 μs), i.e., acquisition started 8 samples early, the phantom image was again faithfully reconstructed (Fig. 6b), but rotated counter-clockwise by a small angle (the readout

gradients traversed 2D *k*-space counter-clockwise). Similarly, a delay of −8 samples caused a slight clockwise rotation of the reconstructed phantom image (Fig. 6c).

These results demonstrate that timing delays only cause a bulk rotation of the reconstruction, which does not degrade the quality of the image. In practice, the delays observed are less than ±8 samples and cause at most a very small rotation. If desired, these small delays can be measured and accounted for in the reconstruction by a simple rotation.

IR-SPGR Brain Imaging

Volumetric whole-brain datasets were obtained with the 3D stack-of-rings IR-SPGR sequence using an 8-channel head coil. Scans were performed with the previously discussed protocols **A** (TI/TD = 600/0 ms, T_{scan} = 4 min 52 s) and **B** (TI/TD = 900/600 ms, T_{scan} = 7 min). The SPGR readout parameters were TE/TR/θ = 1.9 ms/12 ms/15°, readout bandwidth of ±125 kHz, and readout window of 5.6 ms for all rings. Each ring was acquired over 3 revolutions (1.9 ms/revolution) to enable fat/water separation (18). Two repetitions of the outer loop were used to establish a stable signal level before the actual data acquisition started (6). Five dummy readout TRs with the RF excitation pulse and encoding gradients turned off were also inserted in TI right before acquisition to stabilize eddy currents, as is often done for centric-ordered 3DFT sequences (2,5).

Images of the same axial slice are shown in Fig. 7 for both 3D stack-of-rings scans. Good white/gray matter CNR is observed and uniform fat/water separation is obtained over the whole brain for both protocols. Protocol **B** has higher SNR, as expected. The actual measured SNR and CNR values are listed in Table 1.

For comparison, we acquired a 3DFT dataset for the same FOV and resolution in the same scan session using a product IR-SPGR sequence with TI/TD = 600/0 ms (same values as in 3D stack-of-rings protocol **A**), readout bandwidth of ±32.25 kHz, and readout TE/TR/θ = 2.8 ms/6.6 ms/8° (parameters were adapted from (7,24)). This product sequence partitioned *k*-space into P = 480 segments (Q = 90 phase encodes per segment) and had a total scan time of 9 min 34 s. One-dimensional centric ordering was employed in the slice direction (180 slices / 90 = 2 segments for each k_z value) and all corners of *k*-space were acquired with this product sequence.

Representative axial, coronal, and sagittal images are displayed in Fig. 8 to compare the 3D stack-of-rings to the product 3DFT scan. For 3D stack-of-rings, only the separated water images were considered for comparison. ROIs were drawn manually in corresponding regions of each dataset to assess the SNR and CNR quantitatively. Four ROIs in homogenous areas of white matter and six ROIs encompassing cortical gray matter and the caudate nucleus were selected from axial images (22). The noise level was measured from the image background. As listed in Table 1, the calculated values are SNR_{WM} = 24.07 and CNR = 8.86 (η = 37%) for the 3DFT scan, SNR_{WM} = 25.78 and CNR = 12.05 (η = 47%) for 3D stack-of-rings protocol **A**, and SNR_{WM} = 33.46 and CNR = 16.19 (η = 48%) for 3D stack-of-rings protocol **B**. The 3D stack-of-rings scan using protocol **A** required roughly half the scan time of the 3DFT sequence, while achieving higher CNR and higher contrast efficiency. Protocol **B** required a slightly longer scan time than protocol **A**, but was still faster than the product sequence and achieved the highest SNR and CNR levels of the three.

Discussion

The 3D stack-of-rings trajectory inherits the desirable properties of the 2D concentric rings (17,18) and offers even more flexibility in designing the acquisition strategy for efficient magnetization-prepared imaging. As demonstrated in the *in vivo* brain experiments, the 3D

stack-of-rings scan using protocol **A** can achieve higher SNR and higher CNR within a shorter scan duration when compared to a product 3DFT scan using the same TI and TD for the same imaging volume. This scan time advantage can be used for further enhancement of SNR and CNR by performing multiple signal averages, encoding a larger imaging volume, or incorporating longer preparation and recovery time periods, as in protocol **B**. The higher contrast efficiency η for 3D stack-of-rings also means that any overall increase in signal level will be translated into an increase in CNR with greater effect.

Both 3D stack-of-rings imaging protocols were designed to achieve contrast efficiency η on the order of 30%, but in fact the measured values were on the order of 45%. This increase in the actual calculated η may be due to several reasons. First of all, the theoretical value of η is based on particular values of T_1, T_2, and ρ, which represents an average value. Second, we find that η increases as the excitation angle θ decreases, thus nonuniform RF fields can affect the actual η. Although the expected and measured values of η do not agree perfectly, the general trends of SNR and CNR are predicted very well with the simulations.

To gain a better understanding of the advantage of the 3D stack-of-rings trajectory in capturing contrast and mitigating spatial blurring, let us consider a comparison with 1D centric-ordered 3DFT based on theoretical calculations. Suppose both trajectories utilize the same preparation module, the same readout sequence parameters, the same isotropic voxel size, the same image matrix size, and the same $Q = 90$ encoding steps per preparation segment. Let us also assume that the contrast decays to 70% of the prepared level in 30 encoding steps (representative of our imaging experiments). For 3DFT with 1D centric ordering in the slice direction and 2 segments for each k_z value (as in our experiments), the 70%-level volume is a slab of width $2 \cdot (30/90) \cdot k_{max} = (2/3)k_{max}$. On the other hand, the 3D centric-ordered stack-of-rings distributes this volume as a sphere of radius $\sqrt[3]{30/90} \cdot k_{max} = 0.69 k_{max}$. That is, the 70%-level 3DFT slab covers areas of k_x and k_y outside of the central region of k-space, while the 70%-level 3D stack-of-rings sphere covers the central region compactly to maximize contrast. The 70%-level sphere also distributes the contrast decay isotropically in all directions, thus avoiding concentration of spatial blurring along one particular dimension. Since the 70%-level sphere has a diameter that is twice the width of the 70%-level slab in the slice direction, the 3D stack-of-rings trajectory is essentially twice as tolerable to spatial blurring in this direction. The compact spherical geometry of the 3D centric-ordered stack-of-rings trajectory is the source of its advantages for magnetization-prepared imaging.

We have tried to keep most of the imaging parameters consistent for the 3D stack-of-rings and product 3DFT scans, but a direct comparison between the two is not simple. TI and TD were purposely kept the same for 3D stack-of-rings protocol **A** and the product 3DFT sequence so that both experienced the same degree of magnetization preparation. The value of Q could not be explicitly prescribed for the product 3DFT sequence, and was set to 90 by its internal calculations based on the acquisition matrix size. We tested a few different values of Q for the 3D stack-of-rings sequence and decided on 120 as it allowed some reduction of scan time and did not cause visible blurring. While Q was not the same for these two scans, they were both on the order of $Q = 100$ to allow for a meaningful comparison. The main difference between the two sequences is that a larger flip angle of $\theta = 15°$ was used for the 3D stack-of-rings to increase SNR while $\theta = 8°$ was used for the product 3DFT sequence (a popular choice (7, 24)). We did try increasing θ to 15° to increase SNR for the product 3DFT scan, but observed blurring along the one centric-ordered direction and an overall loss of image contrast (results not shown). This is because the product 3DFT sequence concentrated the larger signal modulation due to a larger flip angle in only one centric-ordering dimension, while the 3D stack-of-rings could distribute this modulation isotropically in three dimensions to mitigate loss of image contrast and resolution. For the product 3DFT sequence, TD was not alterable; therefore, we could not compare a product 3DFT scan with TI/TD = 900/600 ms to the 3D

stack-of-rings scan using protocol **B**. Doing so would also have pushed the scan time of the product 3DFT sequence over the desired 10 minute duration. Although there are differences in the exact parameter values for the 3D stack-of-rings and product 3DFT scans, the experimental results shown here still illustrate the advantages of 3D stack-of-rings for magnetization-prepared imaging.

The product IR-SPGR 3DFT sequence used for comparison here was chosen for its wide clinical acceptance and availability, as evidenced by its selection as one of the core sequences in a comprehensive imaging study (24), and also for its role as a baseline standard in many publications (5–7). It may be possible to enhance 3DFT-based acquisitions with square-spiral 2D centric ordering for improved contrast (6) and cylindrical *k*-space coverage for additional scan time savings (7). However, the 3D stack-of-rings trajectory is already able to perform centric ordering in all three dimensions and supports spherical coverage for greater time savings. It would be interesting to perform a comparison with these other investigative sequences in the future.

Although other fast 3D imaging trajectories, such as under-sampled 3DPR or 3D stack-of-spirals, can potentially achieve an even greater reduction in scan time for magnetization-prepared imaging, they are more sensitive to timing delays and off-resonance effects. These trajectories also over-sample the center of *k*-space, which can provide robustness to motion, but can result in mixed or unexpected image contrast for magnetization-prepared imaging (17,25). Compared to these other trajectories, the 3D stack-of-rings can enhance magnetization-prepared imaging while being robust to system imperfections. Since all rings are acquired with a constant angular velocity, timing delays only result in a bulk rotation of the reconstruction. Furthermore, the time-efficient retracing design for concentric rings resolves field inhomogeneities and allows for the reconstruction of separate fat and water images. This is particularly useful for brain imaging, since it automatically suppresses ringing artifacts that may arise from the motion of bright fat signal in the scalp, which becomes enhanced by the use of phased arrays (26). Other 3D concentric trajectories, such as the 3D concentric cylinders (27) and the 3D spherical shells (28) have also been applied to magnetization-prepared imaging. A detailed comparison of these different 3D concentric trajectories for magnetization-prepared imaging in the future would be very beneficial.

In this work, we have implemented and shown the effectiveness of 3D stack-of-rings for the particular case of magnetization-prepared brain imaging. The design principles discussed here can be extended to the design of efficient magnetization-prepared imaging in general and also to the closely related 3D fast spin-echo sequence (29). There are many complementary strategies that can further improve the current design. The use of an optimized series of variable readout excitation angles can allow more encoding steps Q to be acquired per preparation segment, reducing P and scan time while preserving image resolution and contrast (6,22). Variable-density sampling can be easily implemented along k_z and in (k_x, k_y) for additional time savings (30). Furthermore, parallel imaging can be combined with the 3D stack-of-rings trajectory to accelerate the acquisition. In its current form, 1D sensitivity encoding can be utilized along the slice-encoding direction with straightforward Cartesian techniques. Slightly more complicated is the use of sensitivity encoding to complement in-plane circular encoding. Most interesting is the possibility of full 3D parallel imaging, where a small compact sphere can be obtained in the center of *k*-space for calibration purposes. It would be of great interest to explore these design extensions.

Conclusion

We have demonstrated that the 3D stack-of-rings non-Cartesian readout trajectory enables robust and efficient volumetric magnetization-prepared imaging. The 3D stack-of-rings can be

acquired with centric ordering in three dimensions and supports spherical *k*-space coverage. In addition, timing delays only cause a bulk rotation of the reconstruction and each ring can be acquired using a retracing design to resolve off-resonance effects. Experimental results show that the prepared tissue contrast can be captured effectively within a short scan time.

Acknowledgments

The authors thank Jin Hyung Lee for helpful discussions.

This work was supported by NIH, GE Healthcare.

References

1. Haase A. Snapshot FLASH MRI: applications to T1, T2, and chemical-shift imaging. Magn Reson Med 1990;13:77–89. [PubMed: 2319937]
2. Mugler JP III, Brookeman JR. Rapid three-dimensional T1-weighted MR imaging with the MP-RAGE sequence. J Magn Reson Imaging 1991;1:561–567. [PubMed: 1790381]
3. Edelman RR, Wallner B, Singer A, Atkinson DJ, Saini S. Segmented TurboFLASH: method for breath-hold MR imaging of the liver with flexible contrast. Radiology 1990;177:515–521. [PubMed: 2171014]
4. Semelka RC, Willms AB, Brown MA, Brown ED, Finn JP. Comparison of breath-hold T1-weighted MR sequences for imaging of the liver. J Magn Reson Imaging 1994;4:759–765. [PubMed: 7865934]
5. Deichmann R, Good CD, Josephs O, Ashburner J, Turner R. Optimization of 3-D MP-RAGE sequences for structural brain imaging. NeuroImage 2000;12:112–127. [PubMed: 10875908]
6. Stöcker T, Shah NJ. MP-SAGE: A new MP-RAGE sequence with enhanced SNR and CNR for brain imaging utilizing square-spiral phase encoding and variable flip angles. Magn Reson Med 2006;56:824–834. [PubMed: 16947341]
7. Lin C, Bernstein MA. 3D magnetization prepared elliptical centric fast gradient echo imaging. Magn Reson Med 2008;59:434–439. [PubMed: 18183604]
8. Epstein FH, Mugler JP III, Cail WS, Brookeman JR. CSF-suppressed T2-weighted three-dimensional MP-RAGE MR imaging. J Magn Reson Imaging 1995;4:463–469. [PubMed: 7549212]
9. Wilman AH, Riederer SJ. Improved centric phase encoding orders for three-dimensional magnetization-prepared MR angiography. Magn Reson Med 1996;36:384–392. [PubMed: 8875408]
10. Simonetti OP, Finn JP, White RD, Laub G, Henry DA. Black blood T2-weighted inversion-recovery MR imaging of the heart. Radiology 1996;199:49–57. [PubMed: 8633172]
11. Fellner F, Holl K, Held P, Fellner C, Schmitt R, Böhm-Jurkovic H. A T1-weighted rapid three-dimensional gradient-echo technique (MP-RAGE) in preoperative MRI of intracranial tumours. Neuroradiology 1996;38:199–206. [PubMed: 8741186]
12. van den Hauwe L, Parizel PM, Van Goethem JW, De Schepper AMA. Clinical usefulness of contrast-enhanced MP-RAGE of the brain. Neuroradiology 1996;38:S14–S19. [PubMed: 8811673]
13. Atkinson DJ, Edelman RR. Cineangiography of the heart in a single breath hold with a segmented TurboFLASH sequence. Radiology 1991;178:357–360. [PubMed: 1987592]
14. Holsinger AE, Riederer SJ. The importance of phase-encoding order in ultra-short TR snapshot MR imaging. Magn Reson Med 1990;16:481–488. [PubMed: 2077339]
15. Matsui S, Kohno H. NMR imaging with a rotary field gradient. J Magn Reson 1986;70:157–162.
16. Zhou X, Liang ZP, Gewalt SL, Cofer GP, Lauterbur PC, Johnson GA. A fast spin echo technique with circular sampling. Magn Reson Med 1998;39:23–27. [PubMed: 9438433]
17. Wu HH, Lee JH, Nishimura DG. MRI using a concentric rings trajectory. Magn Reson Med 2008;59:102–112. [PubMed: 17969074]
18. Wu HH, Lee JH, Nishimura DG. Fat/water separation using a concentric rings trajectory. Magn Reson Med 2009;61:639–649. [PubMed: 19097243]
19. Reeder SB, Wen Z, Yu H, Pineda AR, Gold GE, Markl M, Pelc NJ. Multicoil Dixon chemical species separation with an iterative least-squares estimation method. Magn Reson Med 2004;51:35–45. [PubMed: 14705043]

20. Bernstein MA, Fain SB, Riederer SJ. Effect of windowing and zero-filled reconstruction of MRI data on spatial resolution and acquisition strategy. J Magn Reson Imaging 2001;14:270–280. [PubMed: 11536404]
21. Silver MS, Joseph RI, Hoult DI. Highly selective π/2 and π pulse generation. J Magn Reson 1984;59:347–351.
22. Epstein FH, Mugler JP III, Brookeman JR. Optimization of parameter values for complex pulse sequences by simulated annealing: application to 3D MP-RAGE imaging of the brain. Magn Reson Med 1994;31:164–177. [PubMed: 8133752]
23. Constantinides CD, Atalar E, McVeigh ER. Signal-to-noise measurements in magnitude images from NMR phased arrays. Magn Reson Med 1997;38:852–857. [PubMed: 9358462]
24. Jack CR Jr, Bernstein MA, Fox NC, Thompson P, Alexander G, Harvey D, Borowski B, Britson PJ, Whitwell JL, Ward C, Dale AM, Felmlee JP, Gunter JL, Hill DLG, Killiany R, Schuff N, Fox-Bosetti S, Lin C, Studholme C, DeCarli CS, Krueger G, Ward HA, Metzger GJ, Scott KT, Mallozzi R, Blezek D, Levy J, Debbins JP, Fleisher AS, Albert M, Green R, Bartzokis G, Glover G, Mugler J, Weiner MW. The Alzheimer's Disease Neuroimaging Initiative (ADNI): MRI methods. J Magn Reson Imaging 2008;27:685–691. [PubMed: 18302232]
25. Peters DC, Botnar RM, Kissinger KV, Yeon SB, Appelbaum EA, Manning WJ. Inversion recovery radial MRI with interleaved projection sets. Magn Reson Med 2006;55:1150–1156. [PubMed: 16598720]
26. Howarth C, Hutton C, Deichmann R. Improvement of the image quality of T1-weighted anatomical brain scans. NeuroImage 2005;29:930–937. [PubMed: 16153861]
27. Rupert, K.; Oshio, K.; Guenther, M.; Mugler, JP, III. An interleaved cylindrical *k*-space trajectory for rapid 3D GRE acquisitions. Proceedings of the 11th ISMRM; Toronto, Ontario, Canada. 2003. p. 208
28. Shu Y, Riederer SJ, Bernstein MA. Three-dimensional MRI with an undersampled spherical shells trajectory. Magn Reson Med 2006;56:553–562. [PubMed: 16894580]
29. Busse RF, Brau ACS, Vu A, Michelich CR, Bayram E, Kijowski R, Reeder SB, Rowley HA. Effects of refocusing flip angle modulation and view ordering in 3D fast spin echo. Magn Reson Med 2008;60:640–649. [PubMed: 18727082]
30. Tsai CM, Nishimura DG. Reduced aliasing artifacts using variable-density *k*-space sampling trajectories. Magn Reson Med 2000;43:452–458. [PubMed: 10725889]

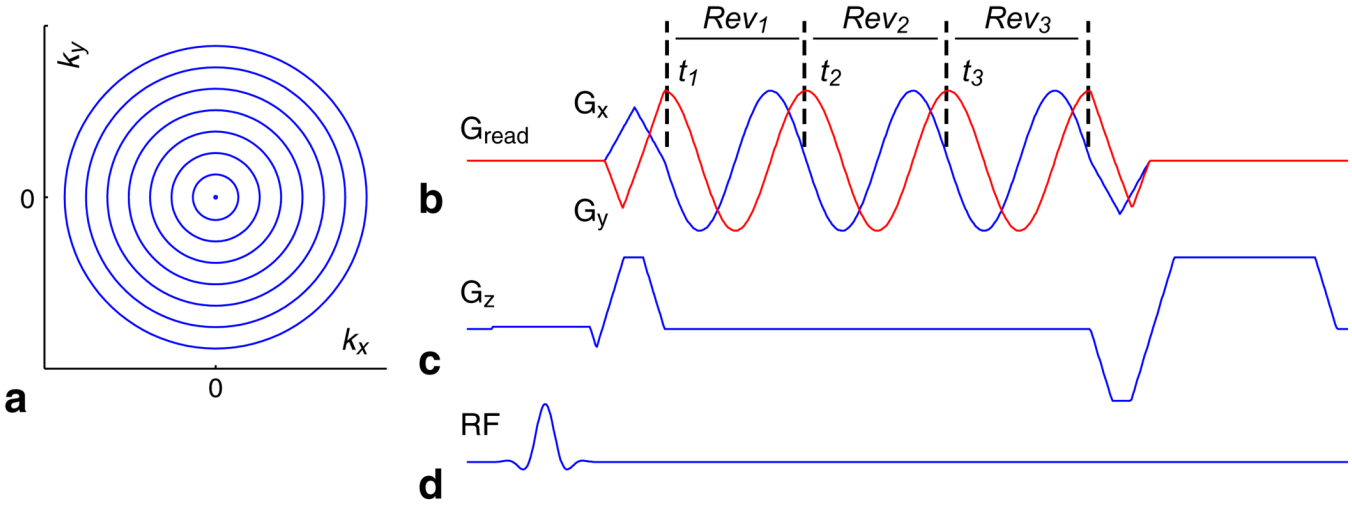

FIG. 1.

3D stack-of-rings pulse sequence. 2D *k*-space is sampled with *N* uniformly spaced concentric rings (a), where sinusoidal gradients are designed for the outermost ring (b) and then scaled down to acquire one ring after each RF excitation pulse (d). Slice encoding gradients (c) are implemented for 3D spatial coverage. A time-efficient retracing design is used to acquire each ring through multiple revolutions (b). Similar to multi-echo acquisitions, each revolution Rev_m captures the image at a different time t_m to enable fat/water separation (m = 1, 2, 3).

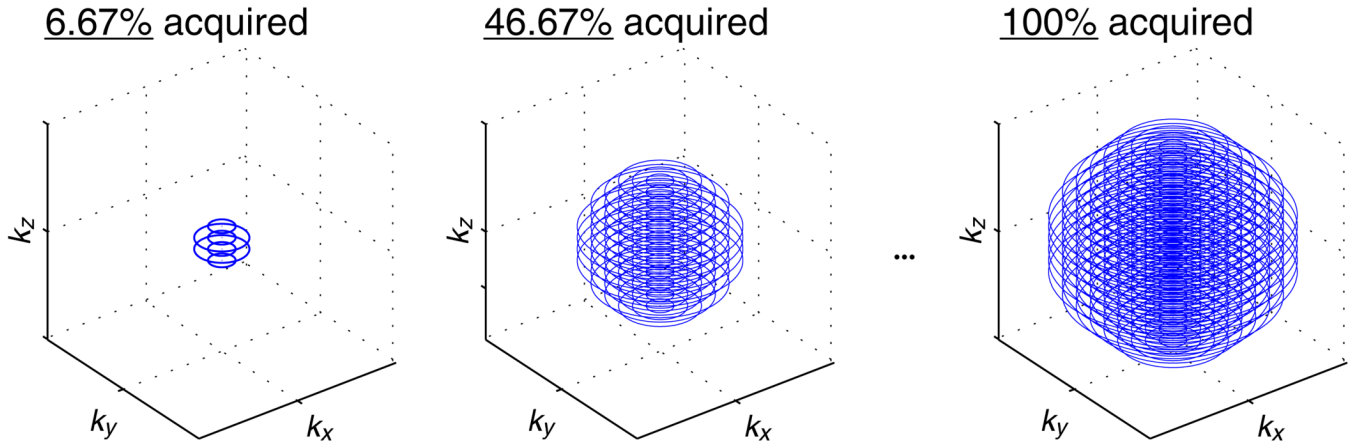

FIG. 2.

3D centric ordering and spherical coverage. The 3D stack-of-rings can be acquired with centric ordering in all three spatial dimensions and supports spherical coverage in 3D *k*-space for additional time-savings while maintaining isotropic spatial resolution. The central region of *k*-space is covered very rapidly using only a small fraction of the full set of samples, thus ensuring that the intended contrast is captured very effectively at a desired point in time.

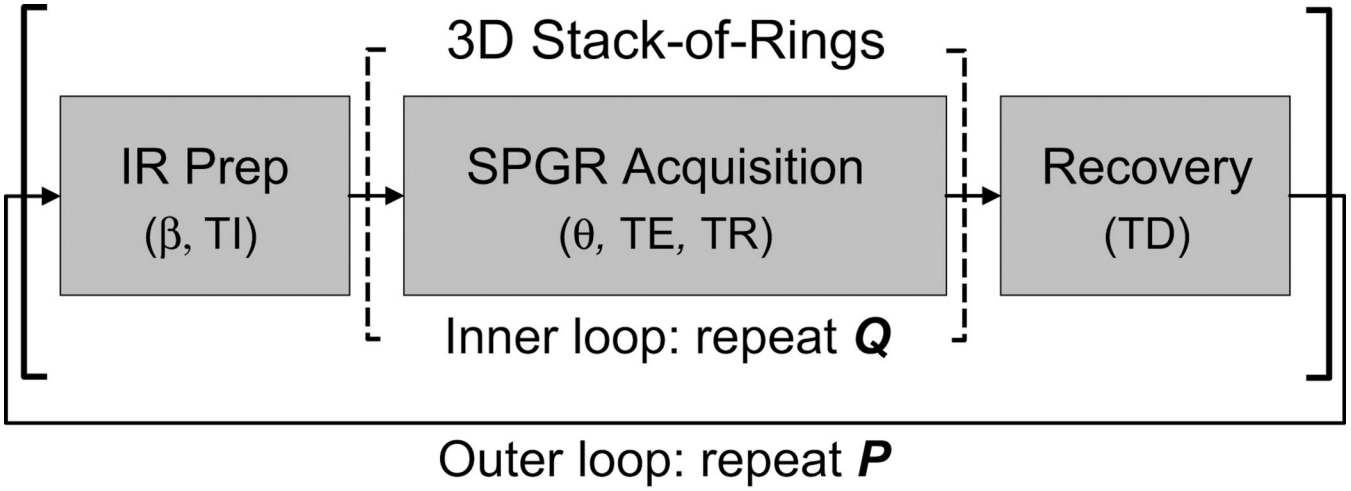

FIG. 3.

IR-SPGR pulse sequence. This sequence consists of three main blocks. An RF pulse with angle β first inverts the magnetization. After observing an inversion evolution time TI, *Q k*-space encoding steps are acquired to capture the intended contrast. Parameters for the SPGR acquisition module include excitation angle θ, excitation time TE, and repetition time TR. In this work, the 3D stack-of-rings with spherical coverage is used for readout. Finally, a recovery delay period TD allows the magnetization to return to equilibrium before the next preparation segment. This whole prepare-acquire-recover loop is repeated *P* times such that $P \cdot Q$ equals the desired set of encoding steps.

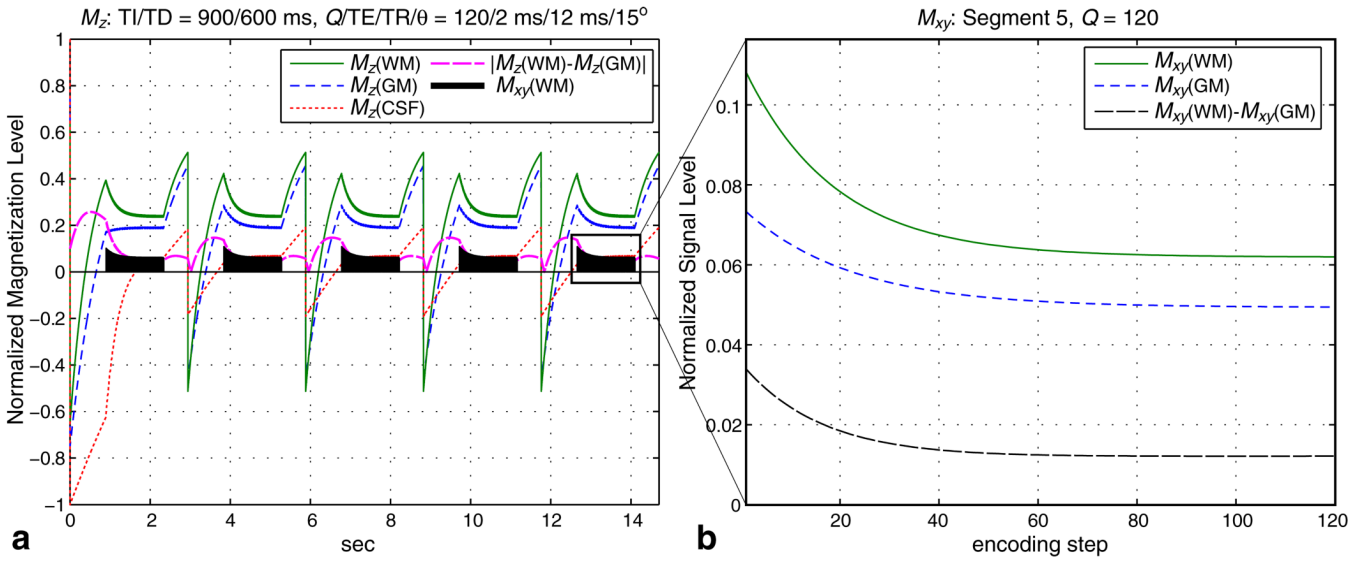

FIG. 4.

Bloch simulation for IR-SPGR. We calculated the signal evolution for GM, WM, and CSF using typical parameters TI/TD = 900/600 ms and Q/TE/TR/θ = 120/2 ms/12 ms/15° (a). The signal evolution stabilizes after about two full cycles of the prepare-acquire-recover outer loop. During the acquisition segment, WM/GM signal difference starts out high because of the preparation, but decays away with each readout (b). The magnetization levels are normalized such that CSF magnetization at equilibrium equals 1.

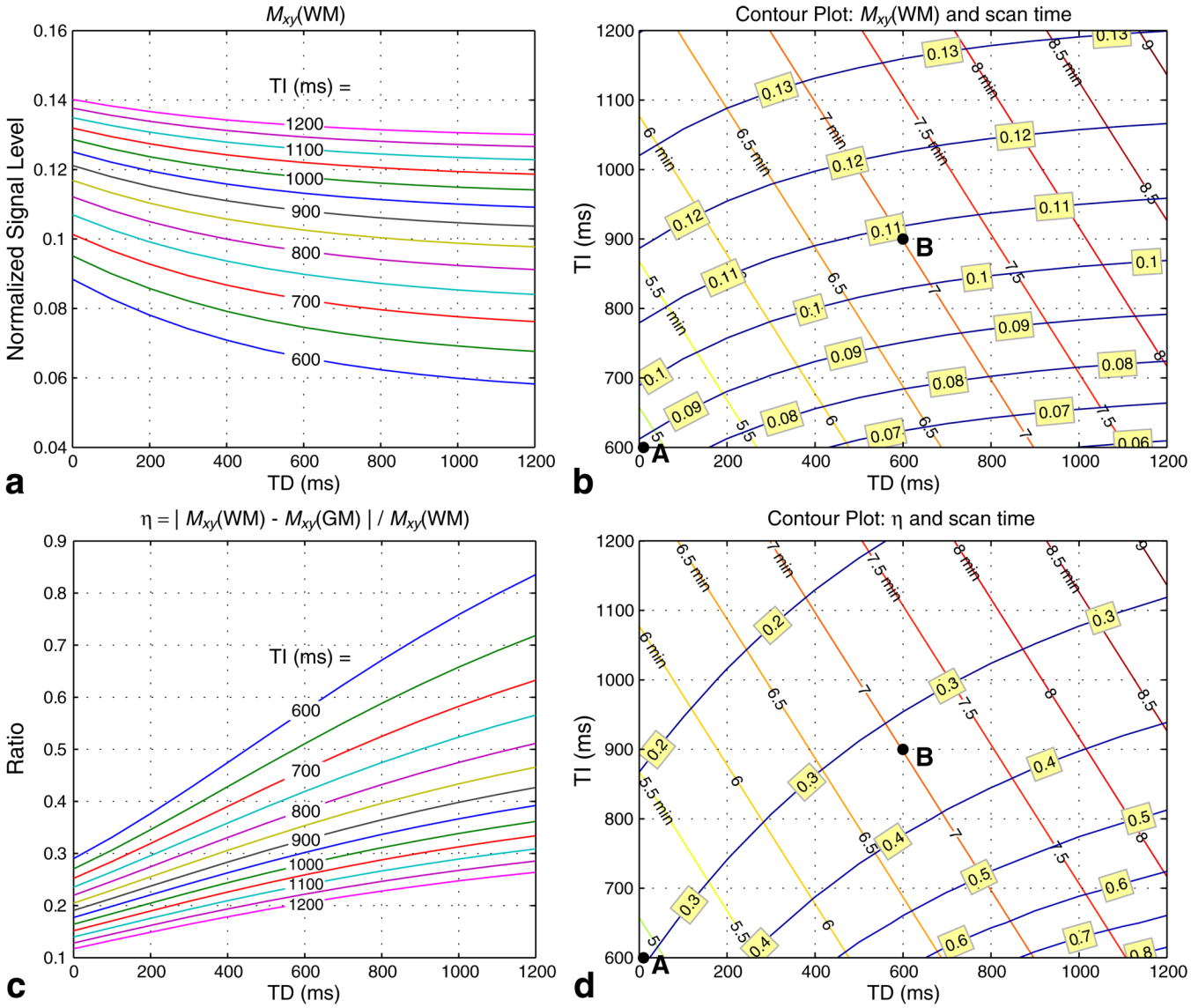

FIG. 5.

Contour plots of sequence trade-offs. Bloch simulations were performed for TI = 600–1200 ms (in steps of 50 ms) and TD = 0–1200 ms (in steps of 100 ms) with Q/TE/TR/θ = 120/2 ms/12 ms/15°. Signal levels for WM and GM from the first encoding step of the readout segment were recorded. M_{xy}(WM) is proportional to SNR_{WM} (a, b), while the contrast efficiency η = | M_{xy}(WM) − M_{xy}(GM)|/M_{xy}(WM) is proportional to CNR/SNR_{WM} (c, d). Contour plots (b) and (d) include the scan time T_{scan} required for whole-brain coverage for each combination of TI and TD. Two protocols were chosen to balance SNR, CNR, and scan time: protocol **A** (TI/TD = 600/0 ms, T_{scan} = 4 min 52 s) is a fast scan while protocol **B** (TI/TD = 900/600 ms, T_{scan} = 7 min) achieves higher SNR. Both protocols theoretically achieve η on the order of 30%.

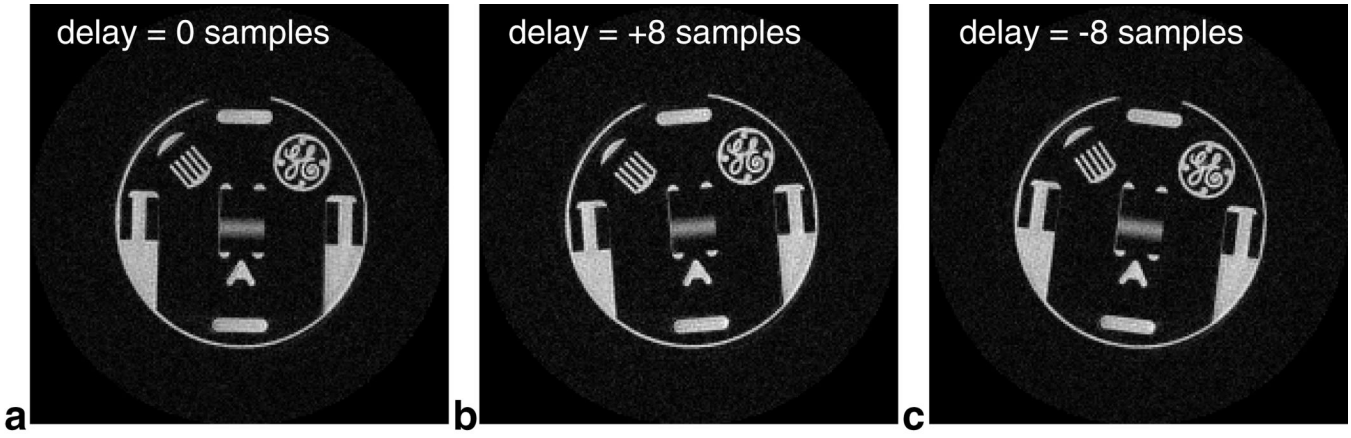

FIG. 6.

Timing delays cause a rotation. When the default calibrated gradient-to-acquisition delay is used, the reconstruction faithfully depicts the phantom, as expected (a). Relatively large delays of +8 and −8 samples were intentionally introduced in (b) and (c). Since all concentric rings are acquired with a constant angular velocity, timing delays only cause a bulk rotation of the reconstructed image and do not degrade the image quality.

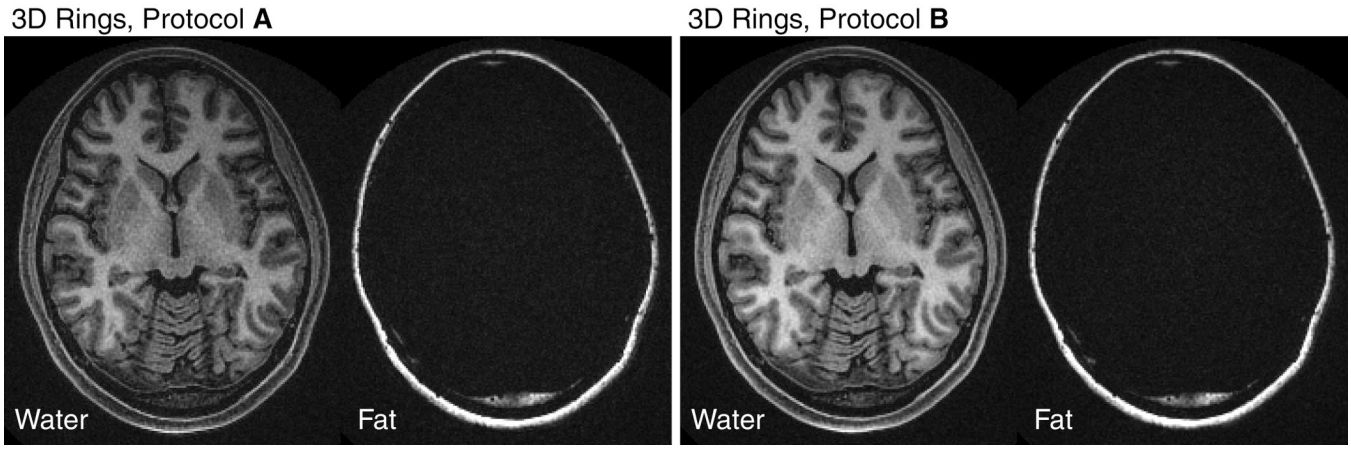

FIG. 7.

3D stack-of-rings IR-SPGR fat-water-separated axial head images. The same brain volume was imaged with both protocol **A** and **B**. Good WM/GM CNR is observed and uniform fat/water separation is obtained over the whole brain for both protocols. Shown here is the central axial slice from both scans. Results from protocol **B** have higher SNR, as expected. The actual measured values are listed in Table 1.

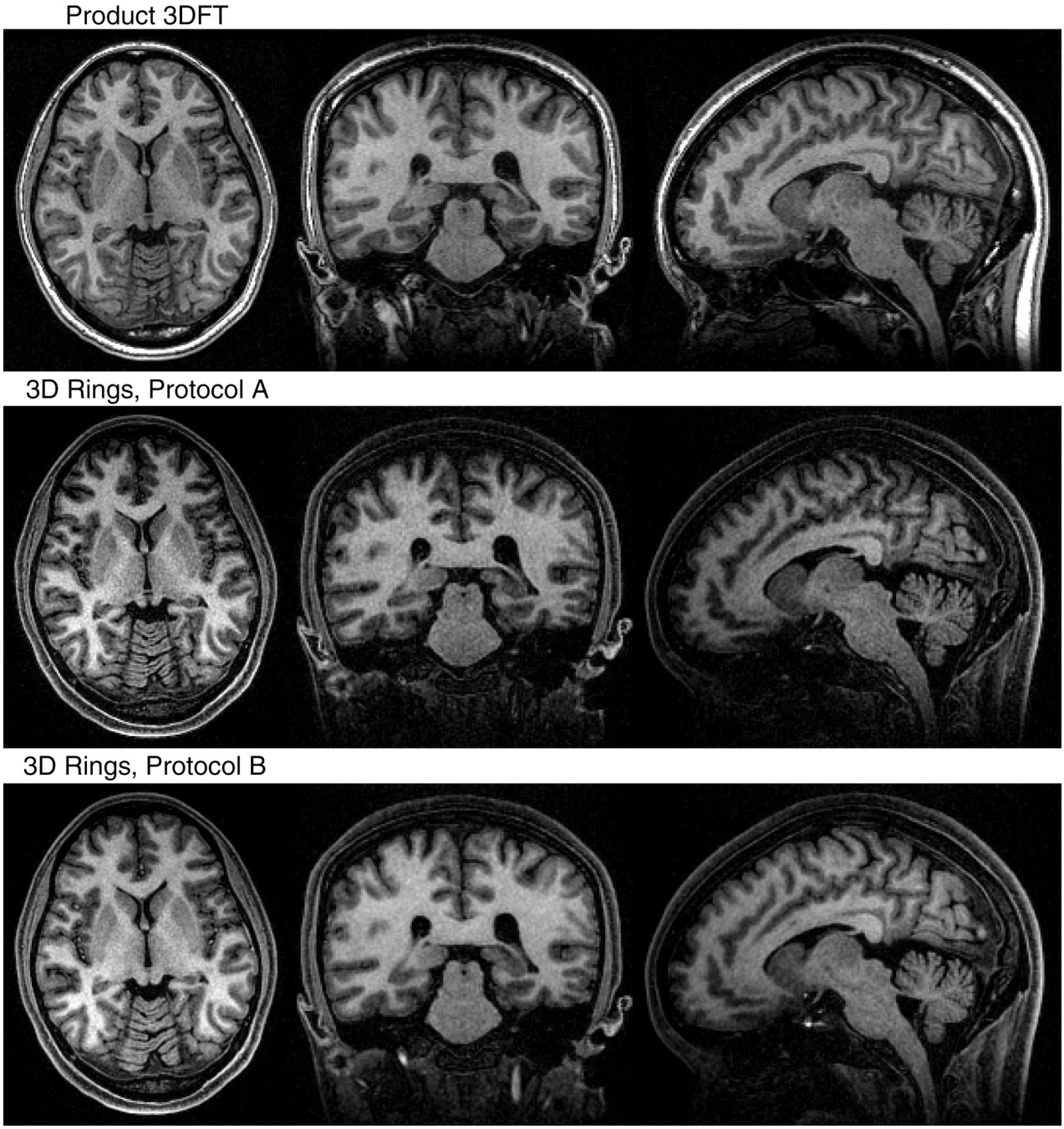

FIG. 8.

Comparison of 3DFT and 3D stack-of-rings scans for the same volume. In addition to protocols **A** and **B**, we also imaged the same brain volume using a product 3DFT IR-SPGR sequence. Only the reconstructed water images were used for comparison for the 3D stack-of-rings scans. Representative axial, coronal, and sagittal slices of the same position are displayed here. All scans show good WM/GM contrast. ROIs were localized in homogeneous areas of white matter and regions of cortical gray matter and the caudate nucleus for quantitative analysis. The 3D stack-of-rings scan using protocol **A** required roughly half the scan time of the 3DFT sequence, while achieving higher CNR and higher contrast efficiency. Protocol **B** required a slightly longer scan time than protocol **A**, but was still faster than the product sequence and achieved

the highest SNR and CNR levels of the three. The actual measured values are listed in Table 1.

Table 1

SNR and CNR measurements.

	Product 3DFT	3D Rings Protocol A	3D Rings Protocol B
TI/TD	600/0 ms	600/0 ms	900/600 ms
T_{scan}	9 min 34 s	4 min 52 s	7 min 00 s
SNR_{WM}	24.07	25.78	33.46
SNR_{GM}	15.21	13.73	17.27
CNR	8.86	12.05	16.19
η	37%	47%	48%